A Climatology of Surface Radiation Budget Derived from Satellite Data

SHASHI K. GUPTA, NANCY A. RITCHEY, ANNE C. WILBER, AND CHARLES H. WHITLOCK

Analytical Services and Materials, Inc., Hampton, Virginia

GARY G. GIBSON AND PAUL W. STACKHOUSE JR.

Atmospheric Sciences Division, NASA/Langley Research Center, Hampton, Virginia

(Manuscript received 23 June 1998, in final form 19 November 1998)

ABSTRACT

Climatological averages of surface radiation budget parameters, namely, the shortwave and longwave surface radiative fluxes, have been derived for each month of the year on a global scale. These climatological averages were derived from an 8-yr (96 month) time series of monthly average fluxes. The monthly averages were computed using fast radiation parameterizations and satellite data from the International Satellite Cloud Climatology Project and the Earth Radiation Budget Experiment. Results are presented as time series of hemispheric and global averages and as geographical distributions and time–latitude cross sections of climatological averages. The spatial/temporal variabilities of the results were found to be clearly related to the corresponding variabilities of meteorological and other inputs to the parameterizations. Numerous comparisons of the present results were made with available surface measurements for the purpose of validation. In most cases, the differences were found to be within the uncertainties of the measurements. In some cases, where they were large, the differences were attributable to identifiable deficiencies in the meteorological inputs and/or the surface measurements. However, large differences remained unexplained in a few cases. Anomalies of shortwave and longwave surface fluxes during the 1986/87 El Niño–Southern Oscillation episode show a strong relationship with corresponding top-of-atmosphere anomalies derived from an independent data source. Comparisons with results from several general circulation models showed large differences, but, in most cases, these were attributable to well-recognized deficiencies in model simulations. Global annual average downward and net shortwave fluxes were found to be about 185 and 161 W m^{-2}, respectively. These values are 10–20 W m^{-2} lower than those obtained from the general circulation models, but they are in good agreement with other satellite-derived estimates. Global annual average downward and net longwave fluxes were found to be about 348 and -48 W m^{-2}, respectively, which are about 10–15 W m^{-2} higher than corresponding values from general circulation models. Atmospheric shortwave absorption derived from the present results is 10–15 W m^{-2} larger than from the general circulation models, but it is in good agreement with another estimate based on satellite data.

1. Introduction and background

The surface radiation budget (SRB), consisting of the downward and upward fluxes of shortwave (SW) and longwave (LW) radiation, is a major component of the energy exchanges between the atmosphere and the land/ocean surface. Surface radiative fluxes affect temperature fields and fluxes of sensible and latent heat, and they play an important role in oceanic and atmospheric general circulation (Ramanathan 1986; Wild et al. 1995). SRB data can be a valuable resource for initializing and validating the general circulation models (GCMs) of the ocean and the atmosphere (Suttles and Ohring 1986). Developing a long-term climatology of SRB is essential to accomplishing the objectives of a number of World Climate Research Program (WCRP) projects, such as the International Satellite Land Surface Climatology Project and the Global Energy and Water Cycle Experiment, which are designed to address outstanding questions in various areas of weather and climate (Suttles and Ohring 1986; Schmetz 1989). Recognizing the scientific value of SRB data, the WCRP initiated the SRB Climatology Project (WCRP-69 1992) with the objective of facilitating and monitoring the development of a reliable long-term climatology of surface radiative fluxes.

Recognition of the scientific potential of SRB led to the creation of an SRB program at the National Aeronautics and Space Administration (NASA)/Langley Research Center (LaRC) during the last decade. The objective of this program was to develop algorithms for producing SRB data on a global scale, preferably using input data from operational satellite sources. The em-

Corresponding author address: Dr. Shashi K. Gupta, Analytical Services and Materials, Inc., One Enterprise Parkway, Suite 300, Hampton, VA 23666-5845.
E-mail: s.k.gupta@larc.nasa.gov

phasis on global coverage led to the choice of meteorological data from the Television Infrared Observational Satellite (TIROS) Operational Vertical Sounder (TOVS) system flown aboard the National Oceanic and Atmospheric Administration's (NOAA) polar-orbiting satellites. The LaRC SRB group developed parameterized LW and SW algorithms for computing all SRB components using TOVS data (Darnell et al. 1983, 1986, 1988; Gupta 1983, 1989). After the introduction of the International Satellite Cloud Climatology Project (ISCCP) data in the late 1980s, which provided high-quality cloud analyses on a global scale, the LaRC SRB group restructured their algorithms to take advantage of this resource (Darnell et al. 1992; Gupta et al. 1992). Physical and semiempirical SRB algorithms were also developed by many other research groups (e.g., Tarpley 1979; Gautier et al. 1980; Pinker and Ewing 1985; Schmetz et al. 1986). However, most of these algorithms did not provide all components of SRB or global coverage, and some relied heavily on surface-measured and/or climatological data for inputs.

Another approach for deriving SRB suggested by some research groups is to establish correlations between radiative fluxes at the top of atmosphere (TOA) and at the surface and then to derive surface fluxes directly using the satellite measurements of TOA fluxes (Ramanathan 1986). It was demonstrated by Cess et al. (1991) and Li et al. (1993) that such correlations worked quite well for surface SW fluxes under clear and cloudy conditions. Presently, however, there is serious controversy regarding a very basic premise underlying these correlations, namely, that additional absorption of SW radiation in clouds (above that in the clear atmosphere) is very small. Analyses and observations by Cess et al. (1995), Ramanathan et al. (1995), and Pilewskie and Valero (1995) suggest strong additional SW absorption in the clouds, while studies by Chou et al. (1995), Li et al. (1995), and Arking et al. (1996) demonstrate that additional SW absorption in the clouds is quite small. While this controversy may be resolved in the future by measurement programs like the Atmospheric Radiation Measurement program's Enhanced Shortwave Experiment, it creates serious uncertainty regarding the reliability of the correlations for producing surface SW fluxes. Correlations for deriving surface LW fluxes from TOA LW measurements have also found only limited use. Stephens et al. (1994) demonstrated a method for deriving climatological values of surface LW flux over ice-free oceans for clear-sky conditions. Their algorithm is based on a ratio of the surface to TOA LW fluxes as a function of column water vapor. For cloudy-sky conditions, the TOA and surface LW fluxes are almost completely decoupled (Stephens and Webster 1984; Schmetz 1989).

This paper presents a time series of monthly averages and monthly climatologies of all components of the SRB derived from ISCCP data and the algorithms developed by the LaRC SRB group (Darnell et al. 1992; Gupta et al. 1992). The length of this dataset is limited to the available record of ISCCP-C1 datasets, which cover 8 yr (July 1983–June 1991). A brief description of the ISCCP-C1 datasets is given in section 2. Section 3 provides a brief description of the SW and LW algorithms. Time series of global and hemispheric averages and analyses of the spatial and temporal characteristics of SRB are presented in section 4. Comparisons of these results with surface-measured data are provided in section 5. Section 6 presents comparisons of the climatological averages of these data with corresponding averages from several GCMs. An analysis of errors is given in section 7. Section 8 presents the concluding remarks and information on the availability of this dataset to the scientific community.

2. Input data

Satellite data from the ISCCP and the Earth Radiation Budget Experiment (ERBE; Barkstrom et al. 1989) were used as inputs to the present SRB algorithms. ISCCP-C1 datasets (hereafter C1 data) were produced by the NASA/Goddard Institute for Space Studies and are archived at the LaRC Distributed Active Archive Center (DAAC). The C1 data provide cloud parameters derived from a network of geostationary satellites and NOAA's polar orbiters, along with temperature and humidity profiles from TOVS, on a 2.5° equal-area global grid and a 3-hourly time resolution (Rossow et al. 1988; Rossow and Schiffer 1991). The cloud parameters derived from geostationary satellite radiances over most of the globe are updated every 3 h. A surface temperature value (the clear-sky composite surface temperature) was also derived from geostationary satellite radiances and updated every 3 h. Ancillary meteorological data obtained from TOVS (temperature and humidity profiles and column ozone) were updated only once every day. Monthly average clear-sky planetary albedos used for deriving surface albedos over snow/ice-free land areas were obtained from ERBE data, which are also archived at the LaRC DAAC.

3. Radiation models

Radiation models used for computing surface fluxes were developed over the years and are documented in the literature (Darnell et al. 1988, 1992; Gupta 1989; Gupta et al. 1992). A brief outline of the models is presented in this section. Minor modifications made to the SW model since its publication are reported in the appendix. All flux computations were made on a grid-box basis.

a. SW model

The SW model described in detail by Darnell et al. (1988, 1992) is a physical parameterization in which the overall transmittance of the atmospheric column is

computed from clear-sky and cloud transmittances, which are computed separately. In the clear-sky portion of the parameterization, the overall extinction of SW radiation is computed by adding contributions from gaseous absorption, Rayleigh scattering, and aerosol absorption and scattering. Aerosol extinction is computed using climatological values of optical depths and other radiative properties for each of the five different scene types used in this work (see appendix). The current aerosol model represents an improvement over the residual method used in Darnell et al. (1992), as it accounts for some of the geographical variability of aerosol extinction. Effects of seasonal variability of background aerosols, or of transient events like biomass burning, are not accounted for in this model because such information is not available. Cloud extinction was computed by a relative threshold method using scaled visible reflectances of C1 data, a process that makes the results less dependent on ISCCP-provided instrument calibration (Whitlock et al. 1995). The direct use of measured reflectances also eliminates the need for explicit accounting of microphysical processes (e.g., cloud SW absorption). Surface albedos for all-sky conditions were derived from a combination of clear-sky and overcast albedos, as well as cloud transmittances. Clear-sky surface albedos for ice-free ocean areas were taken from the literature (Payne 1972). For land areas, monthly average clear-sky surface albedos were derived from ERBE or C1 data depending on the snow/ice condition at the surface (see appendix). Overcast albedos for both ocean and land areas were obtained by modifying the corresponding clear-sky values for diffuse radiation conditions (Darnell et al. 1992).

b. LW model

The LW model, described in detail by Gupta et al. (1992), is a fast parameterization developed from an accurate narrowband radiative transfer model. Downward longwave flux (DLF) is computed in terms of an ''effective emitting temperature'' of the atmosphere, column water vapor burden, fractional cloud amount, and cloud-base height. All these parameters except the cloud-base height can be derived directly from the C1 data. Cloud-base height is estimated using climatological cloud thicknesses from Telegadas and London (1954) in conjunction with satellite-derived cloud-top heights. The effective emitting temperature is a weighted average for the lower layers of the atmosphere, as most of the DLF reaching the surface originates very near the surface (Schmetz et al. 1986; Gupta 1989). Strong correlation between surface temperature and near-surface air temperature allows the use of the former (which is available from C1 data) as a proxy for the latter (which is not available) in the weighting scheme. As a result, surface temperature weighs strongly in the computation of DLF, and temperature-related variability of the DLF is discussed in terms of the surface temperature throughout this paper.

4. Results and discussion

Results are presented as time series of hemispheric and global monthly averages, and geographical distributions and time-latitude plots of 8-yr monthly averages. An example of the interannual variability of surface fluxes associated with the 1986/87 El Niño–Southern Oscillation (ENSO) episode is examined and compared with the corresponding variability of TOA fluxes obtained from ERBE. Broad features of surface fluxes are interpreted in terms of the known distributions of the meteorological variables and of the sensitivities of the surface fluxes to these variables. In the sign convention used here, downward fluxes are positive and upward fluxes are negative.

a. Time series

Figures 1a–d show the time series of the hemispheric and global monthly average fluxes for the entire 96-month period. Figure 1a for downward SW flux shows a strong seasonal cycle for the hemispheric averages. The Southern Hemisphere (SH) shows a slightly larger amplitude related to the facts that (i) the sun–Earth distance is minimum during January (SH summer) and maximum during July, and (ii) the Northern Hemisphere (NH) column water vapor shows a strong seasonal cycle with very large values in the NH during July (Wittmeyer and Vonder Haar 1994). Time series of net SW flux. (Fig. 1b) show similar features with the interhemispheric differences slightly enhanced during July because of higher surface albedos over landmasses of the NH. Global averages of both parameters show a small seasonal variability ($\approx$6 W m^{-2}).

Figure 1c shows the time series of the DLF. The seasonal variability for the NH is far stronger than for the SH. The largest contributor to this variability is the seasonal cycle of surface temperature over the large landmasses of the NH. Recall that surface temperature is used as a proxy for the near-surface air temperature in the DLF computation. Large seasonal variability of column water vapor in the NH (Wittmeyer and Vonder Haar 1994) reinforces this interhemispheric difference. As a result, the global average exhibits a moderate seasonal variability ($\approx$15 W m^{-2}) in phase with the NH average.

Time series of net LW flux (NLF), which represents a heat loss from the surface, are shown in Fig. 1d. Under the sign convention used here, NLF is a negative quantity; its discussion, however, is much more intuitive and convenient when conducted in terms of its magnitude. Both hemispheric averages show seasonal variability in NLF but they are quite different. Because of much higher surface temperature during the NH summer and lower column water vapor during the NH winter, NLF is much larger over the NH throughout the year, with minor ex-

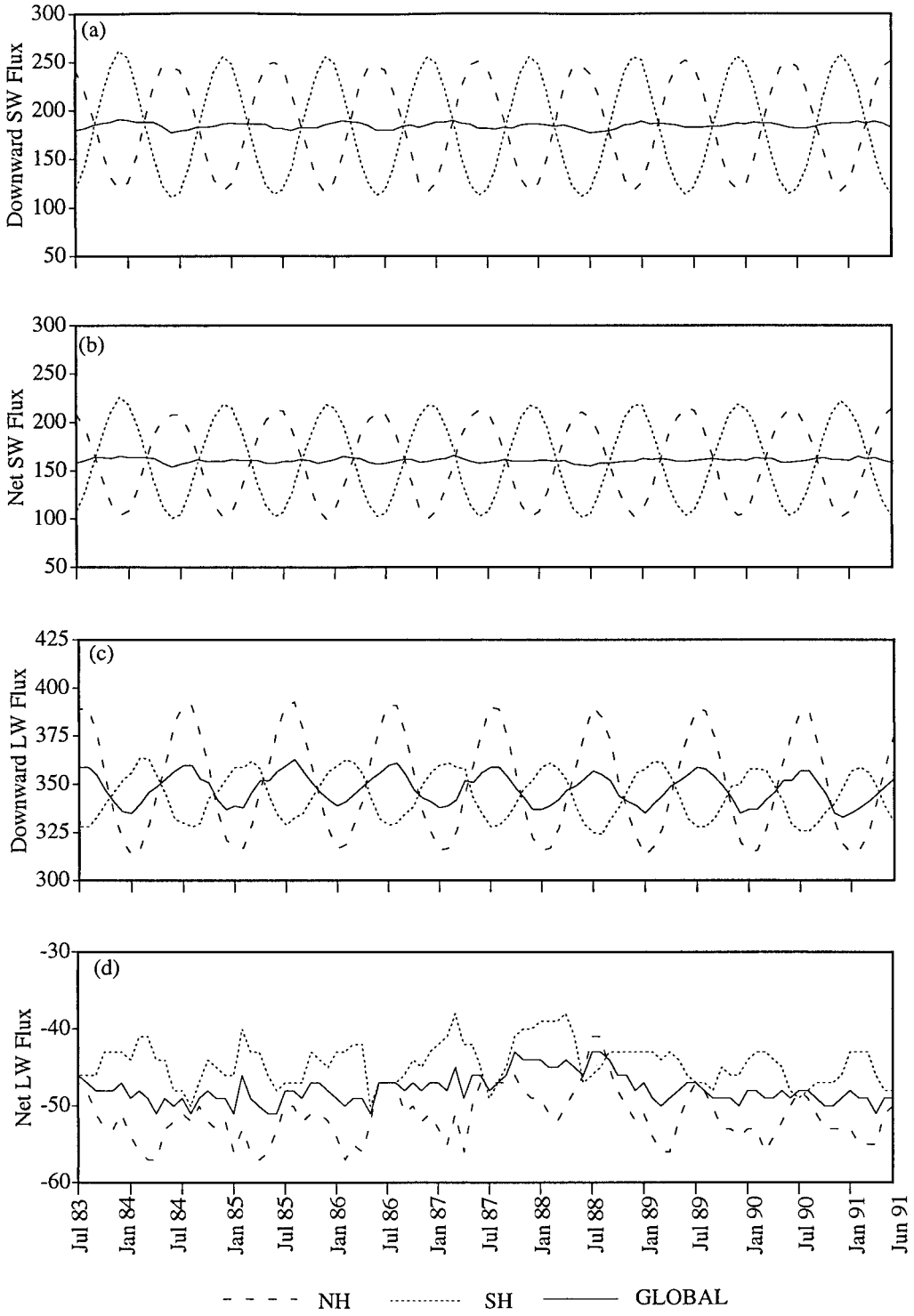

FIG. 1. Time series of monthly average surface fluxes for the 8-yr period: (a) downward SW, (b) net SW, (c) downward LW, and (d) net LW. Fluxes in all figures are expressed in W m^{-2}.

TABLE 1. Hemispheric and global climatological average surface radiative fluxes (W m^{-2}) for January, July, and the whole year from the Langley 8-yr SRB dataset. Numbers in parentheses are standard deviations and represent interannual variabilities of the means.

	NH	SH	Global
	Downward shortwave flux		
Jan	125.2 (1.1)	249.6 (2.1)	187.4 (1.4)
Jul	242.7 (2.7)	118.4 (1.6)	180.6 (2.1)
Annual	186.7 (0.8)	182.6 (1.2)	184.7 (0.9)
	Net shortwave flux		
Jan	108.3 (0.8)	215.6 (1.9)	162.0 (1.1)
Jul	209.4 (2.5)	107.5 (1.4)	158.4 (1.9)
Annual	160.2 (0.8)	161.5 (1.1)	160.9 (0.9)
	Downward longwave flux		
Jan	315.2 (1.9)	358.4 (1.4)	336.8 (1.5)
Jul	389.8 (1.3)	327.9 (1.6)	358.8 (1.3)
Annual	351.0 (1.5)	344.6 (1.7)	347.8 (1.6)
	Net longwave flux		
Jan	−52.8 (2.1)	−42.9 (1.8)	−47.9 (1.9)
Jul	−47.2 (3.0)	−47.1 (1.1)	−47.2 (1.8)
Annual	−51.3 (1.7)	−44.4 (1.3)	−47.9 (1.5)
	Net total (SW + LW) flux		
Jan	55.5 (1.9)	172.7 (2.4)	114.1 (2.0)
Jul	162.2 (2.3)	60.4 (1.5)	111.2 (1.8)
Annual	108.9 (1.7)	117.1 (1.0)	113.0 (1.2)

ceptions. Still, the two hemispheric averages move in opposite phase, and the global average shows a small variability (≈4 W m^{-2}) about the mean. Means and standard deviations over 8 yr of hemispheric and global averages of the above SRB parameters, along with net total fluxes (net SW + net LW) for January, July, and the whole year computed from the entire dataset, are presented in Table 1. Note that these standard deviations are a measure of the interannual variability of the respective means.

b. Geographical distributions

Figures 2a–d show the geographical distribution of the 8-yr averages of downward and net SW fluxes for January and July. Figures 2a,c for the downward SW flux (insolation) show maxima over the subsidence regions and polar areas of the summer hemisphere. Small cloud amounts over subsidence regions and long sunshine hours over polar areas account for these features. Large cloud amounts in the storm tracks account for the much lower values over the midlatitudes of the summer hemisphere. For the winter hemisphere, polar areas do not receive sunlight, and low values over midlatitudes result from a combination of low TOA insolation and dense cloud cover in the storm tracks. Relatively low

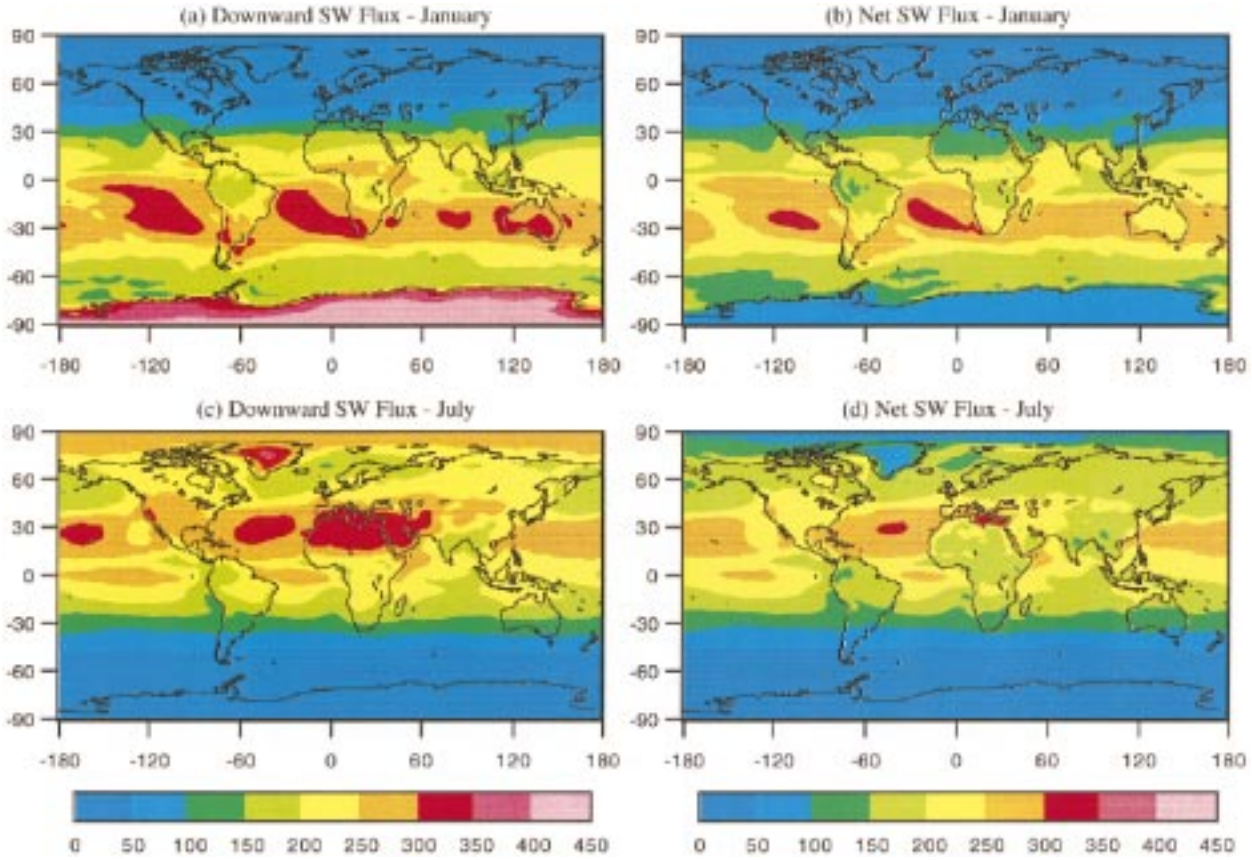

FIG. 2. Geographical distribution of 8-yr average SW fluxes for Jan and Jul: (a), (c) downward and (b), (d) net.

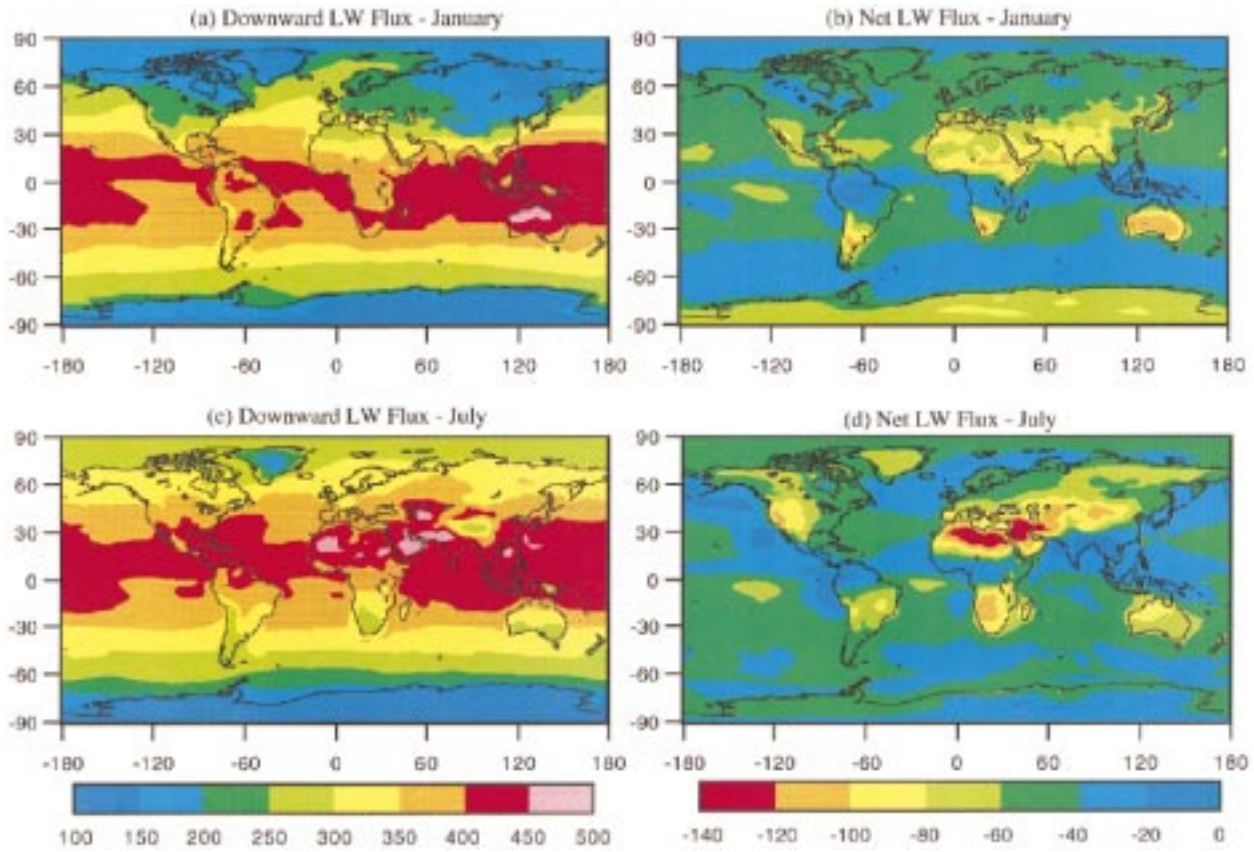

FIG. 3. Geographical distribution of 8-yr average LW fluxes for Jan and Jul: (a), (c) downward and (b), (d) net.

values over the equatorial regions are caused by the cloudiness along the intertropical convergence zone (ITCZ). Figures 2b,d show that net SW fluxes are similar to the downward SW fluxes in Figs. 2a,c. The most important differences occur over deserts and polar areas of the summer hemisphere. Higher surface albedos over these areas result in much lower net SW fluxes. A comparison of the north African desert with the adjacent Mediterranean Sea for July shows that the net SW flux over the desert is about 125 W m^{-2} lower, even though insolation over the two regions is comparable.

Figures 3a–d show geographical distribution of the 8-yr averages of DLF and NLF for January and July. Distribution of DLF in Figs. 3a,c shows broad maxima covering the Tropics and the subtropics, resulting from high temperatures near the surface and high column water vapor content. Cloud effects on DLF are not large for these regions. The very highest values occur over the large desert areas of the summer hemisphere. Low DLF values over the Tibetan plateau and other high-altitude areas result from low surface temperatures and low column water vapor. The broad maximum shifts a little northward from January to July with the shift of the ITCZ. Distribution of NLF in Figs. 3b,d shows maxima over desert regions of the summer hemisphere resulting from the high surface temperatures and small cloud amounts. Prominent minima are located over equatorial regions where large cloud amounts and high column water vapor greatly suppress the NLF.

c. Time–latitude plots

Zonally averaged climatological values of these fluxes and their variability over the seasonal cycle are shown in Figs. 4a–d. Downward SW flux presented in Fig. 4a shows maxima over the subtropics and polar areas of the summer hemisphere. The SH maxima are slightly stronger than those for the NH, due to variation of the Sun–Earth distance. The minima occur over the polar areas and high latitudes of the winter hemisphere. Net SW flux, presented in Fig. 4c, shows some similarities and some differences with downward SW flux. Net SW flux also shows maxima over the subtropics of the summer hemisphere, but interhemispheric contrast is enhanced because of the lower surface albedos in the SH. Polar areas of the summer hemisphere do not show maxima in net SW flux due to very high surface albedos.

The plot for DLF in Fig. 4b shows a broad maximum covering the Tropics and the subtropics, and its seasonal shift toward the summer hemisphere. The larger northward shift during the NH summer is indicative of the strong heating over the Afro-Asian deserts and the cen-

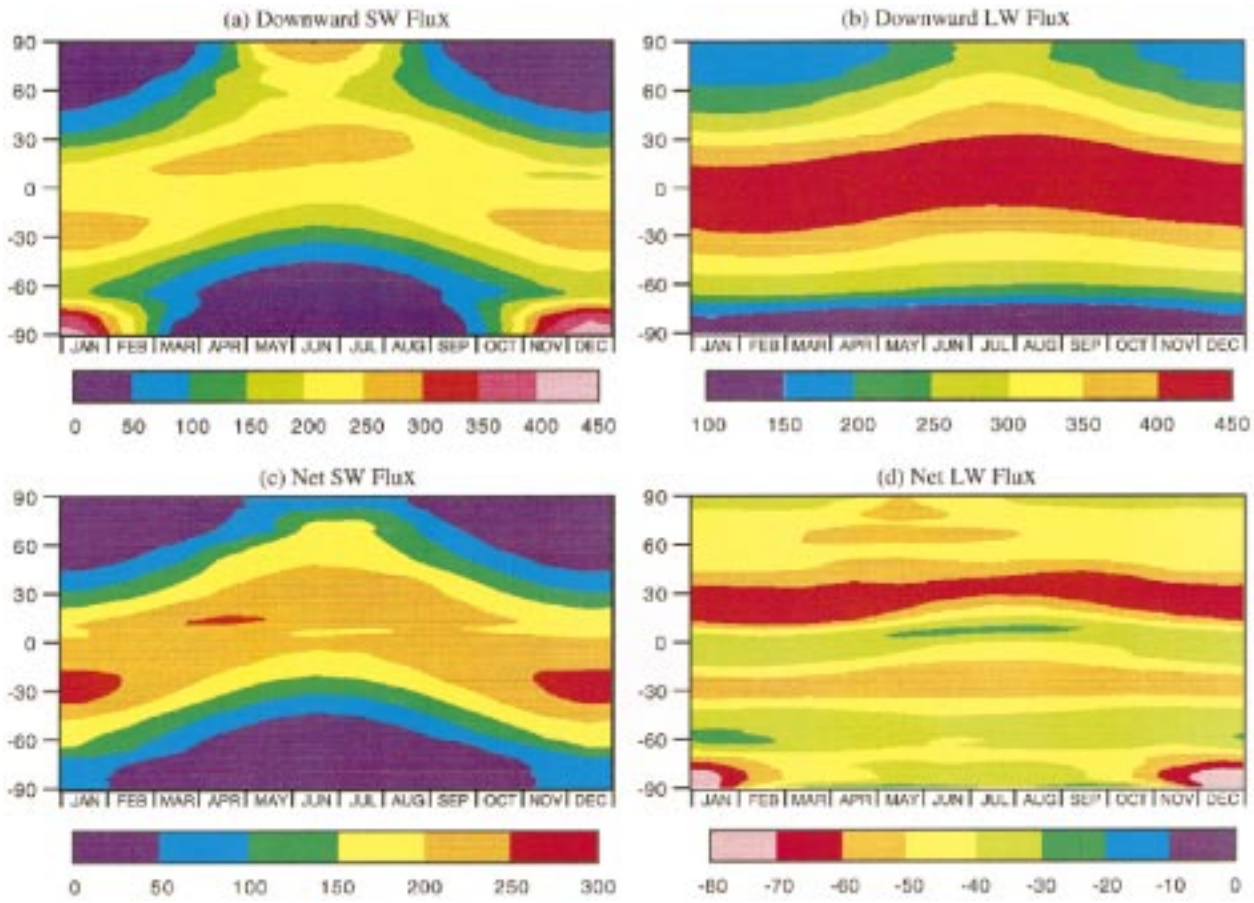

FIG. 4. Time–latitude plots of monthly climatological fluxes (8-yr averages): (a) downward SW, (b) downward LW, (c) net SW, and (d) net LW.

tral Asian landmass. The strong year-round minimum over the SH polar areas is caused by the near absence of moisture over the Antarctic continent due to high elevation. The NLF plot in Fig. 4d shows year-round maxima over the subtropics of both hemispheres, resulting primarily from smaller cloud amounts. The NH maximum is enhanced by low moisture content over the landmasses, especially during the winter. The strong maximum over Antarctica during the SH summer results from surface warming and smaller cloud amounts (in the C1 data) during that season. The minima over the equatorial regions are caused by high moisture content and larger cloud amounts along the ITCZ.

d. Interannual variability

ENSO episodes are among the most important interannual phenomena occurring in the climate system (Trenberth 1997). During the period of this dataset, an ENSO episode of significant magnitude occurred during 1986/87, and it was fully developed by May 1987 (Kousky and Leetmaa 1989). The region of most interest for ENSO is the tropical Pacific Ocean (Philander 1990). Anomalies of net SW and net LW surface fluxes between May 1987 and the 8-yr average for May (1984–91) are presented here to examine the effect of this episode on SRB. Also, the surface anomalies are compared with those in TOA reflected SW and outgoing LW fluxes. The TOA flux anomalies, between May 1987 and the 5-yr average for May (1985–89) were derived by Harrison et al. (1994) from ERBE data.

Figures 5a,b show the spatial distribution of the anomalies for surface net SW and LW fluxes respectively over the tropical Pacific Ocean. The SW anomalies in Fig. 5a show large negative values (-60 to -20 W m^{-2}) close to the equator and positive values (up to 45 W m^{-2}) between 5° and 20° latitude in both hemispheres. Corresponding LW anomalies in Fig. 5b are opposite in sign and considerably smaller in magnitude. Spatial distribution of these anomalies matches closely with corresponding anomalies in the TOA SW and LW fluxes, shown in Figs. 5c,d, respectively. The TOA SW and LW anomalies are also of opposite sign, but their magnitudes are comparable. The TOA anomalies were interpreted by Harrison et al. (1994) in terms of the changes in cloud parameters as shown by ISCCP data.

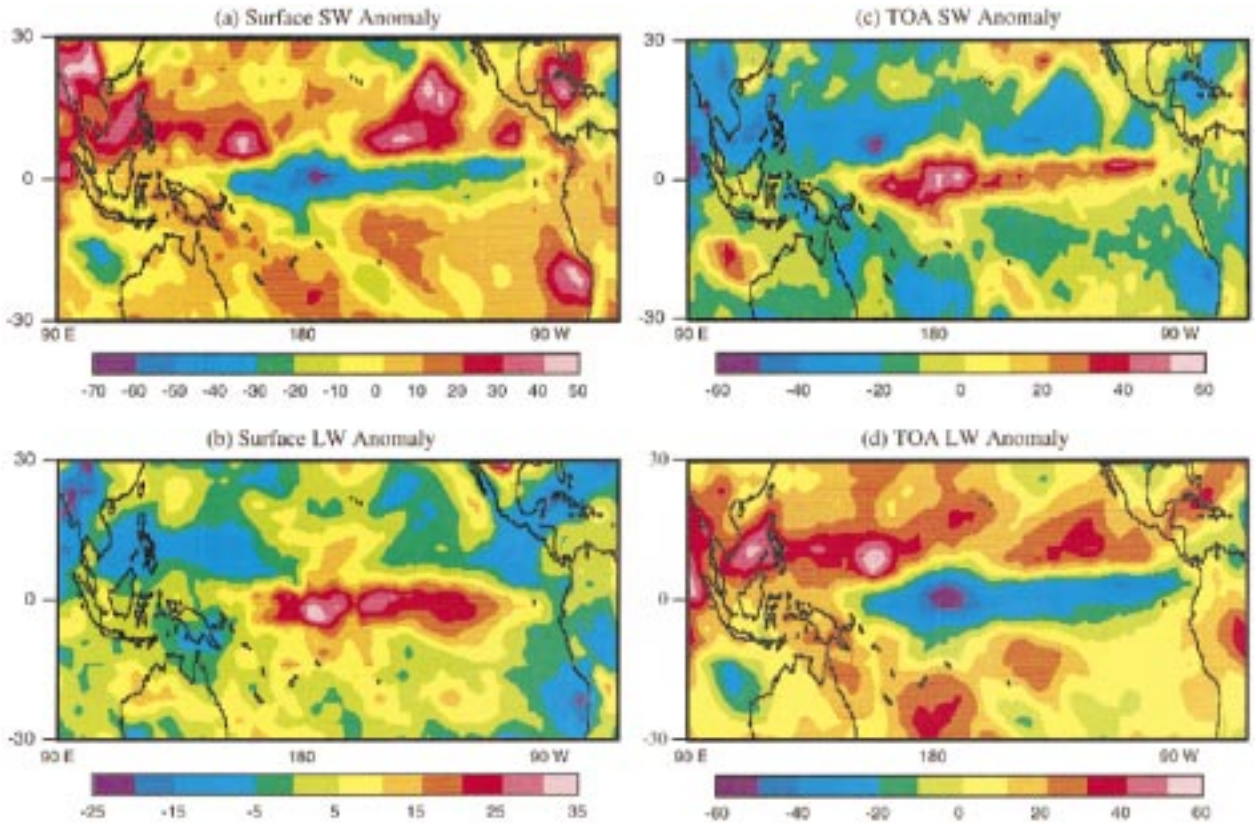

FIG. 5. Distribution of surface flux anomalies for May 1987 over the tropical Pacific Ocean: (a) surface SW, (b) surface LW, (c) TOA SW, and (d) TOA LW.

Important among these changes were the eastward advance of convective activity from the warm pool region to the central and eastern equatorial Pacific and the increase in the amount of high thick clouds over those regions. The difference in the magnitudes of the surface and TOA LW anomalies, as shown in Figs. 5b,d, is consistent with that interpretation because the sensitivity of surface LW fluxes to changes in high thick clouds is much smaller than the sensitivity of TOA LW fluxes.

5. Comparisons with surface-site measurements

Surface fluxes derived in the present work have been compared extensively with site-measured fluxes for the purpose of validating the former. To ensure clarity in the following discussion, the present results will be referred to as satellite fluxes. The choice of sites for which comparisons were made was based largely on the availability of high-quality measurements from those sites. Data quality considerations resulted in the use of site data acquired mainly from three sources—namely, the Global Energy Balance Archive (GEBA) at the Swiss Federal Institute of Technology (Ohmura and Gilgen 1991, 1993), the NOAA/Climate Monitoring and Diagnostics Laboratory (CMDL), and the Commonwealth Scientific and Industrial Research Organization (CSIRO), Australia. Most of the GEBA data used here are SW fluxes from a large number of sites throughout the world. Longwave fluxes were not available from many GEBA sites. The NOAA/CMDL and CSIRO data provided SW and LW fluxes from a few additional sites. Site data from all of the above sources have been processed and used before by other researchers (e.g., Wild et al. 1995; Garratt 1994; Garratt and Prata 1996). These researchers have provided their results to the authors to be used in the present work. Almost all available SW fluxes are insolation fluxes, and LW fluxes (where available) are DLFs. Comparisons are presented as time series of monthly averages for a few sites, as seasonal/annual cycles of multiyear monthly averages for a few other sites, and as scatterplots of monthly averages from many sites.

All such validations necessarily involve comparisons between fluxes measured at a site (which represents a small area) and satellite fluxes derived on a grid-box scale (which represents a large area). Generally, the small area around a site is not representative of a grid box, which may contain terrain features quite unlike the site. Occasionally, a single grid box does not represent the characteristics of a site adequately, especially if the site is located near the edge of the grid box. Efforts to improve comparisons in this regard were tailored to the

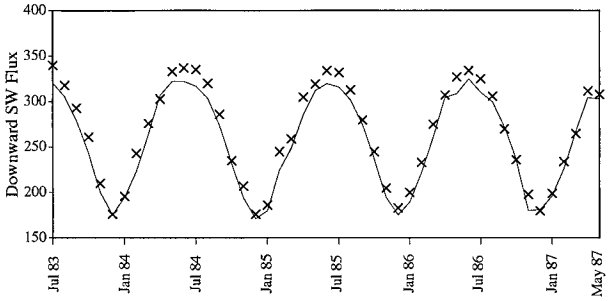

FIG. 6. Comparison of satellite-derived and site-measured downward SW fluxes at Aswan dam, Egypt. In this figure and Figs. 7–10, satellite-derived results are represented by the solid line and site-measured results by the "×" symbol.

specific conditions of each case. In some instances, multiple sites were located in a grid box, and measured fluxes from all such sites were averaged for comparison with the grid-box values. In other cases, satellite fluxes from several adjacent grid boxes were averaged for comparison with measured fluxes from a single site.

a. Time series comparisons

Comparison of insolation data obtained from GEBA for a site at the Aswan dam in Egypt (24.0°N, 32.8°E) with corresponding satellite results for the period July 1983–May 1987 is shown in Fig. 6. The satellite results captured the seasonal cycle well and show good agreement with site fluxes over most of the year with the exception of the summer months. The mean bias and rms difference for these data are 9.6 and 11.6 W m^{-2}, respectively. Another comparison of GEBA insolation data for a site in Payerne, Switzerland, is presented in Fig. 7a. This site is located in the western part of Switzerland (46.8°N, 7.0°E) in a semimountainous region. The comparison shows good agreement over most of the year but significant overestimation in satellite results during the winter months. The mean bias between these data is 12.5 W m^{-2}, and the rms difference is 18.4 W m^{-2}. A record of surface-based estimates of cloud amounts at the site was available from the Swiss Federal Institute of Technology (T. Konzelmann 1993, personal communication). Its comparison with corresponding grid-box average C1 cloud amounts is shown in Fig. 7b. The figure shows fair agreement over the summer months but substantial underestimation in C1 cloud amounts during the winter months. Average cloud amounts for the entire 38-month period from the site and C1 data were found to be 66% and 46%, respectively. For the winter months only (assumed October–March), these averages were even farther apart: 74% for the site and 44% for C1 data. Insolation computed corresponding to the higher cloud amounts would be considerably lower and in better agreement with the site measurements. Figure 7c shows a similar comparison of DLF for the Payerne site. Satellite-derived DLF using

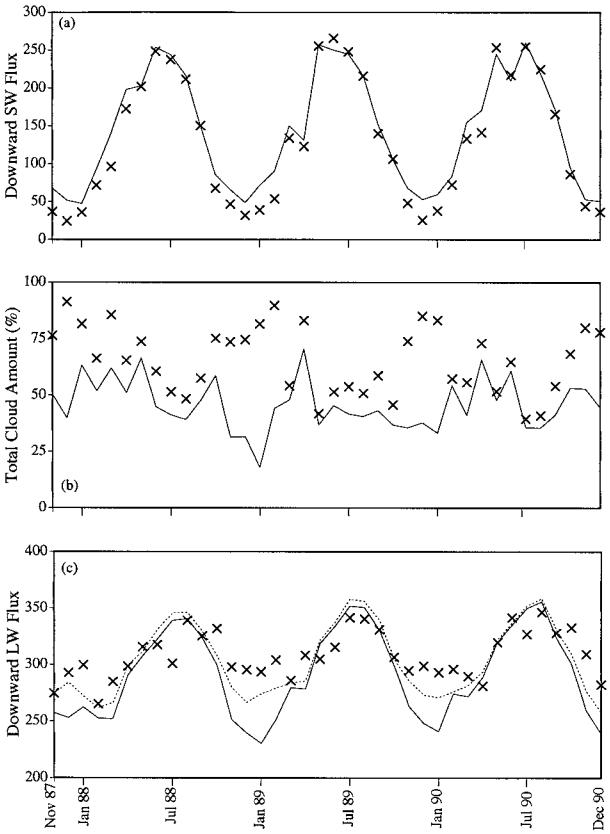

FIG. 7. Comparison of satellite-derived and site-measured results at Payerne, Switzerland: (a) downward SW flux, (b) total cloud amount, and (c) downward LW flux. The dotted line in (c) represents the downward LW flux computed with the surface-based estimates of cloud amounts.

C1 cloud amounts (represented by the solid curve) shows serious underestimation relative to the site-measured DLF (represented by the "×" symbols). However, when site-measured cloud amounts were substituted in the LW model, the recomputed values of satellite DLF (represented by the dotted curve) show much better agreement with the site data. Quantitatively, the mean bias changed from −16.3 to −4.4 W m^{-2}, and the rms difference changed from 29.9 to 18.4 W m^{-2}.

Comparisons with SW and LW fluxes obtained from several of NOAA's radiation monitoring sites through CMDL (E. Dutton 1995, personal communication) are presented below. Figure 8a shows the comparison of insolation from March 1989 to June 1991 for a site at the Kwajalein Islands, located at 10°N in the central Pacific Ocean. The satellite-derived fluxes used here are averages for two adjacent grid boxes, because the islands lie at the boundary between these boxes. Both time series show a weak seasonal cycle, as expected for this latitude; but satellite results overestimate insolation most of the time. Mean bias between the two datasets is 10.3 W m^{-2}, and the rms differences is 19.1 W m^{-2}. Comparison of DLF for Kwajalein for the same period

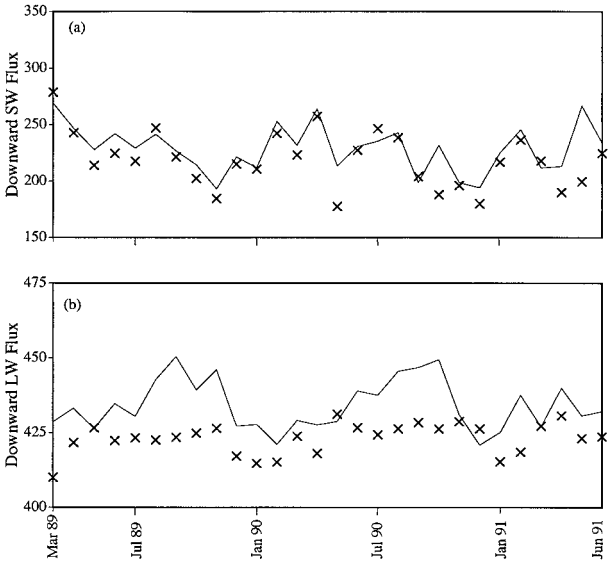

FIG. 8. Comparison of satellite-derived and site-measured fluxes at Kwajalein Island: (a) downward SW and (b) downward LW.

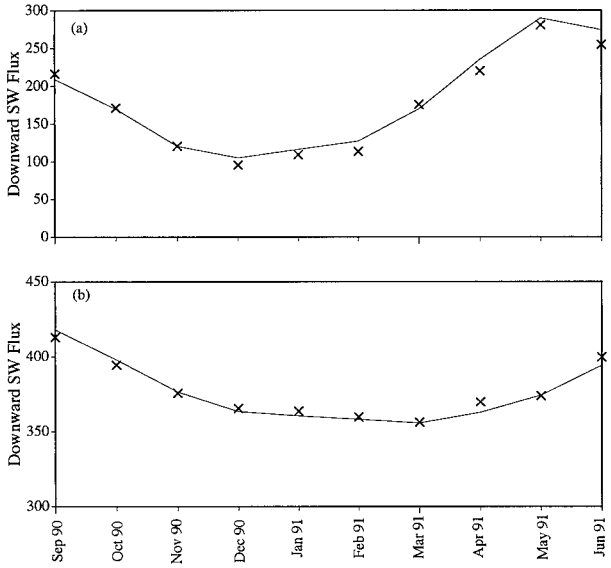

FIG. 9. Comparison of satellite-derived and site-measured fluxes for Bermuda: (a) downward SW and (b) downward LW.

is shown in Fig. 8b. Satellite DLF shows a modest seasonal cycle, while site DLF shows almost none. Mean bias between the two datasets is 11.1 W m^{-2}, and the rms difference is 13.5 W m^{-2}. Further investigation of these differences was not undertaken because ancillary meteorological data from this site were not available to the authors. Comparison of insolation for a site in Bermuda (32.5°N, 66.5°W) from September 1990 to June 1991 is presented in Fig. 9a. This site is located in the extreme northeast corner of a C1 grid box, and in the authors' judgment, the measurements from this site are best represented by the average of satellite-derived fluxes from three adjacent grid boxes. Satellite-derived insolation shows a mean bias of 6.0 W m^{-2} and rms difference of 10.5 W m^{-2}. Corresponding comparison of DLF at the Bermuda site presented in Fig. 9b shows a mean bias of -1.0 W m^{-2} and rms difference of 3.6 W m^{-2}. Figure 10a presents a comparison of insolation values at the South Pole site for the period April 1986–January 1988. Satellite-derived insolation was averaged over three C1 boxes surrounding the pole. Satellite insolation shows some overestimation for all months of sunshine. Mean bias for insolation is 14.7 W m^{-2}, and the rms difference is 26.2 W m^{-2}. Part of this bias may arise from the lower cloud amounts in the C1 data over the South Pole. Comparison of DLF for the South Pole site, presented in Fig. 10b, shows a mean bias of -10.0 W m^{-2} and rms difference of 15.0 W m^{-2}. The figure shows significant underestimation in the satellite DLF during the SH summer but good agreement during the rest of the year. Availability of upward LW flux (ULF) from the site helps to explain these differences in terms of possible errors in surface temperature. Figure 10c shows a comparison of ULF measured at the site and ULF computed from the surface temperatures available

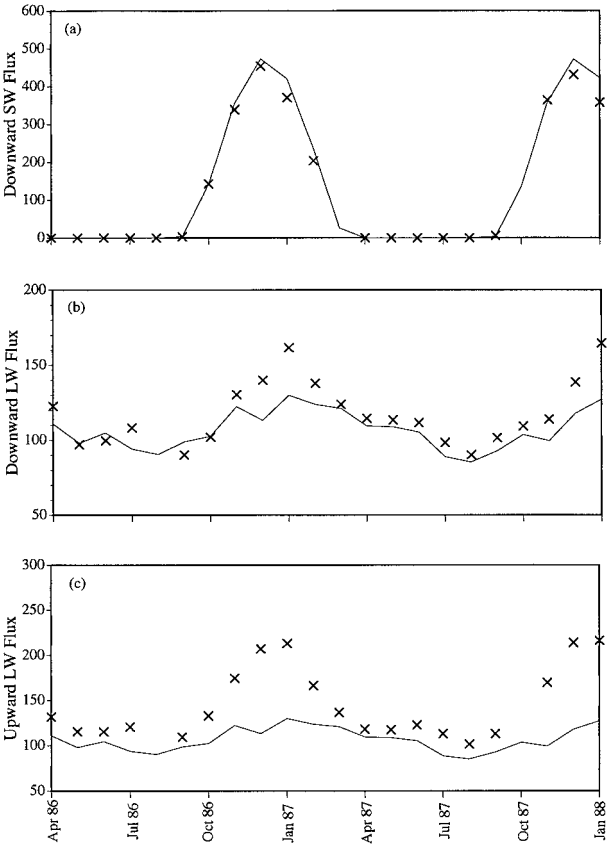

FIG. 10. Comparison of satellite-derived and site-measured fluxes at the South Pole: (a) downward SW, (b) downward LW, and (c) upward LW. The solid line in (c) represents results of a computation using satellite-derived surface temperature.

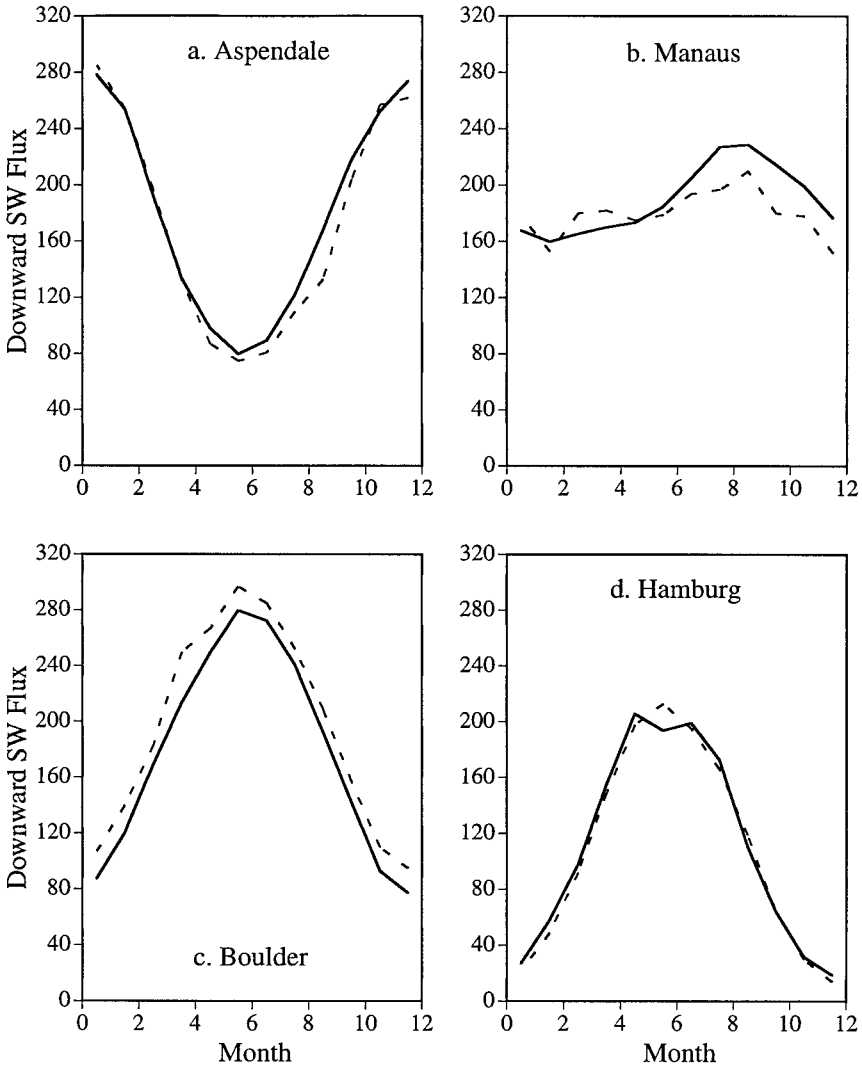

FIG. 11. Comparison of the annual cycle of satellite-derived and site-measured downward SW fluxes at four sites in different climate regimes. Satellite fluxes are 8-yr averages. Averaging periods for the site data are discussed in the text. In this figure and in Fig. 12, satellite results are represented by solid lines and site results by dashed lines.

from C1 data (assuming surface emissivity = 1). The differences indicate that C1 surface temperatures are considerably lower than those at the site during the SH summer. The use of C1 surface temperatures in the satellite algorithm results in the underestimation of DLF.

b. Annual cycle comparisons

Figures 11a–d show comparisons of the annual cycles of site and satellite surface insolation for four sites located in very different climate regimes. The site values (dashed curves) are multiyear averages for each month computed from data records of different lengths and obtained from different sources. These site data are exactly the same as presented by Garratt (1994) in comparisons with GCM results and were provided to the authors by J. Garratt (1998, personal communication). For information on the sources and the lengths of records for these data, the reader is referred to Garratt (1994). The satellite fluxes (solid curves) are 8-yr averages for each month for the C1 grid box in which the site is located. Comparisons for Aspendale, Australia (Fig. 11a) show that the annual cycle of insolation at the site is well captured in the satellite results. There is good agreement for all months except September, when the satellite value exceeds the site value by about 35 W m^{-2}. Mean bias of the satellite results is less than 7 W m^{-2}, and the rms difference is 13 W m^{-2}. For Manaus, Brazil, satellite values significantly exceed the site values for the August–December period. At least part of these differences can be attributed to biomass burning and will be discussed in some detail in the next section.

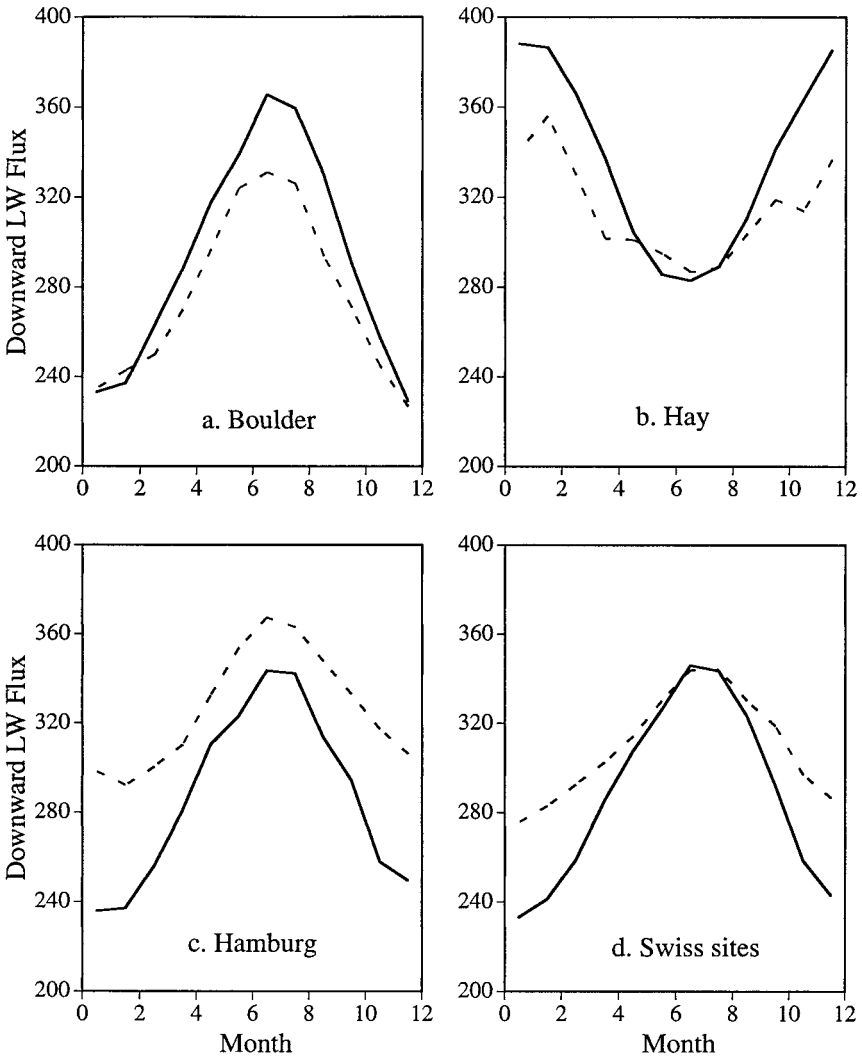

FIG. 12. Comparison as in Fig. 11 for downward LW flux. Note that only two of the four sites are the same as in Fig. 11.

Comparison for Boulder shows significant underestimation throughout the year, and that for Hamburg shows excellent agreement.

Figures 12a–d show similar comparisons of DLF for a set of four sites, two which are the same as used above for SW comparisons. Site data for Boulder and Hay, Australia are the same as presented in Garratt and Prata (1996) and were provided to the authors by J. Garratt (1998, personal communication). Site data for Hamburg are the same as presented in Wild et al. (1995). Figure 12d shows a combined comparison for three sites in Switzerland, which were presented individually in Wild et al. (1995). The data for these sites were provided to the authors by M. Wild (1998, personal communication). Site data for the three Swiss sites were averaged for the present comparison because they are all located in the same C1 grid box. Comparisons for Boulder and Hay show good agreement during local winter but significant underestimation during local summer. The Hamburg comparison shows significant underestimation throughout the year, which is especially large during the winter months. The Swiss sites' comparison shows good agreement during the summer months but significant underestimation during the winter months. The C1 cloud amounts for the grid boxes involved were examined as a potential cause for some of these flux differences. Because coincident measurements of cloud amounts from the sites were not available, C1 cloud amounts were compared with collocated monthly average cloud amounts from the land-cloud climatology of Warren et al. (1986). Cloud amount differences for Boulder and Hay were generally quite small and could not account for the DLF differences. For the Hamburg site, however, C1 cloud amounts were about 20% lower in the annual average and about 30% lower when averaged over the winter months (October–March). Because cloud radia-

tive forcing of DLF for conditions of low moisture content (of the atmosphere) and low clouds (in height) can be quite large (Gupta et al. 1993a), cloud amount differences could account for a large part of DLF differences at Hamburg. The combined comparison for the Swiss sites is quite similar to the time series comparison for the Payerne site presented in the previous section. The C1 cloud amounts were 20%–25% lower over the winter months compared with the Warren et al. (1986) values. These differences can account for a large part of the DLF differences seen over the winter months. Dome heating corrections (Garratt and Prata 1996) are expected to be quite small for both the Hamburg and Swiss sites, especially during the winter months.

c. Scatterplot comparisons

These plots show comparisons of satellite-derived insolation with SW fluxes obtained from GEBA only. Whitlock et al. (1993) performed extensive analyses of the locations of GEBA sites in relation to C1 grid boxes, and they identified 303 C1 boxes with at least one quality-checked GEBA site located in them. Where more than one GEBA site was located in a box, an average value for all GEBA sites was used. Even for C1 boxes with only one site, the spatial-scale mismatch problem was alleviated to some extent because of monthly averaging (temporal averaging compensating for spatial variability). The 303 grid-box dataset provided a total of 13 356 matched box–month data pairs over the 8-yr period of the satellite results. A scatterplot of these data pairs is presented in Fig. 13a, which shows a bias of 5.2 W m^{-2} with a large scatter (rms difference = 24.0 W m^{-2}). A large part of these errors arises from points that have been identified with problem prone areas as discussed below. A group of points showing significant overestimation in satellite fluxes has been identified with regions in South America and Africa where absorbing aerosols from biomass burning are known to decrease surface insolation (Cahoon et al. 1992; Konzelmann et al. 1996). These aerosols have not yet been accounted for in the SW model used in this work and contribute to the positive bias of the satellite estimates. Most other points that contribute to the large scatter come from coastal, desert, or snow/ice-covered sites where satellite-derived fluxes are subject to large uncertaities in cloud amounts and surface albedo. Comparisons from such sites may also be affected by the spatial-scale mismatch between the site and the grid box. A scatterplot of a much more intensive comparison of 234 matched box–month data pairs from three grid boxes over Germany is presented in Fig. 13b. Each grid box included in this comparison contains seven or more GEBA sites. This plot shows a lower bias (4.9 W m^{-2}) and a much lower scatter (rms difference = 11.4 W m^{-2}). These statistics definitely indicate that averages from a number of sites within a box constitute a better representation of the satellite results for that box.

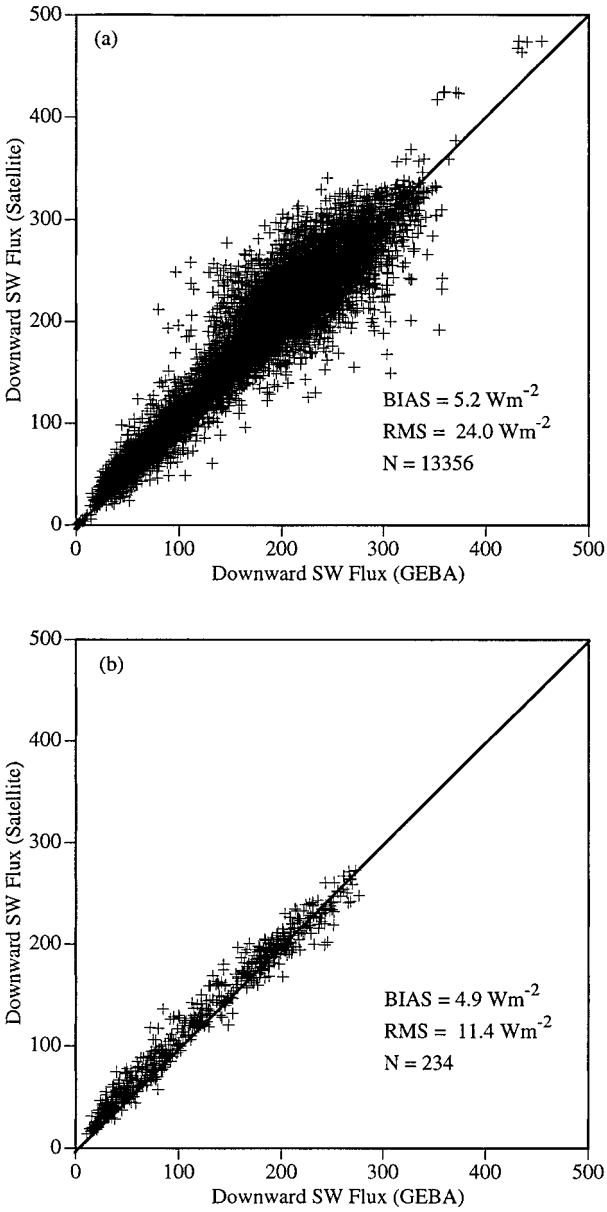

FIG. 13. Scatterplot comparison of matched site (from GEBA) and satellite monthly average downward SW fluxes for the entire 8-yr period: (a) for 303 grid boxes with at least one GEBA site in each box and (b) for three grid boxes over Germany with seven or more GEBA sites in each.

6. Comparisons with GCM results

A potential application of a satellite-derived dataset like the one developed here is in validating the results of GCM simulations (Wild et al. 1995; Ward 1995). Toward that end, SRB parameters available from some widely used GCMs have been compared with the results obtained in this work. The GCMs compared are the Colorado State University GCM (hereafter CSU/GCM), the National Center for Atmospheric Research (NCAR) community climate model version 2 (hereafter CCM2),

and the newest version of the NCAR community climate model, the CCM3. In the following comparisons, results obtained in this work will be used as a reference and referred to as the LaRC results. The comparisons presented here are limited to those between monthly climatological values of zonal, hemispheric, and global averages because of the following considerations. First, the primary emphasis in this work was on climatological averages, and so detailed temporal comparisons were not undertaken. Second, the four datasets involved here use three different spatial grids, and a comparison of geographical distributions would have necessitated a regridding of all datasets to a common grid, with attendant errors. Last, detailed comparisons of several parameters from each of the three GCMs would have stretched this paper beyond a reasonable length. Therefore, such comparisons are best left for future work. Another limitation of these comparisons is that all SRB parameters available from the LaRC dataset were not archived for all GCM runs and thus not available for comparison. Surface insolation was unavailable for the CCM2, and DLF was unavailable for both CCM2 and CCM3. The fields of these parameters were simply not archived at the time of GCM runs even though they were computed. In order to make the desired comparisons, monthly fields of DLF for both CCM2 and CCM3 were recreated from the corresponding fields of surface temperature and NLF, assuming surface emissivity to be unity. No attempts were made to recreate the surface insolation fields for CCM2 because surface albedo fields were not available. All parameters were available from the CSU/GCM.

Comparisons of the zonal averages of downward and net SW and LW fluxes from the GCMs with corresponding LaRC averages are presented in Fig. 14. Each GCM shows differences with LaRC results that arise from the differences between meteorological inputs, the radiation schemes, and radiative properties of the surface and the clouds (Ward 1995). The differences shown in Fig. 14, and those presented later in Table 2, will be discussed in terms of the above characteristics of the GCMs. Geographical distribution of SRB parameters and the meteorological inputs to the radiation scheme of each GCM were examined in detail to interpret these differences, even though they are not included here in the interest of brevity. Comparisons of downward SW flux in Figs. 14a,b (for January and July, respectively) show that GCMs overestimate downward SW flux over most of the globe except near the summer pole. The summer hemisphere differences are much larger than those over the winter hemisphere. Also note that CCM2 results are absent in this comparison. The comparisons of net SW flux shown in Figs. 14c,d are very similar. Comparisons of DLF in Figs. 14e,f show that relative differences are small over most of the globe except near the poles. The dissimilar seasonal variation of DLF over the two hemispheres, noted earlier in the LaRC results, is evident in these figures for all GCMs. The net LW flux comparisons in Figs. 14g,h show that LaRC values are the smallest (in magnitude) and that the relative differences are large. Comparisons of hemispheric and global averages from the GCMs are presented in terms of their differences with the corresponding LaRC values (GCM − LaRC) in Table 2. These differences of climatological averages for January, July, and the whole year are organized in the same format as the results in Table 1. Information specific to a GCM and to the magnitudes of its differences with LaRC results are discussed below separately for each GCM.

a. CSU/GCM

The CSU/GCM results compared here came from simulations for a 10-yr period (January 1979–December 1988) produced for the Atmospheric Model Intercomparison Project (AMIP; Gates 1992). The version of the model used for these simulations is described by Fowler et al. (1996) and Fowler and Randall (1996). It differs from the earlier versions in that the new bulk cloud microphysics scheme encompasses five prognostic variables that link hydrologic processes with radiative processes through parameterizations (Fowler et al. 1996). The dataset was acquired directly from the CSU scientists who developed and ran the model (D. Randall 1997, personal communication). The differences between climatological average SRB parameters for the CSU/GCM and corresponding LaRC averages are presented in the first three columns (of numbers) in Table 2.

Values in Table 2 show that hemispheric/seasonal surface insolation in CSU/GCM exceeds the LaRC values by 4–29 W m^{-2}. In global/annual average the excess is about 17 W m^{-2}. Comparison of net SW fluxes shows differences of about the same magnitude as for insolation. This suggests that the flux differences are primarily due to differences in absorption in the atmospheric column (clear sky and/or clouds) and not due to differences in surface albedos. Excess SW fluxes in the CSU/GCM are also indicative of significant differences between the radiation schemes and cloud radiative properties because they occur in spite of higher column water vapor and much higher cloud amounts in the CSU/GCM compared to the C1 datasets. Hemispheric/seasonal DLF values show differences in the −3 to −11 W m^{-2} range, with a global/annual difference of about −7 W m^{-2}. Corresponding differences for NLF are in the −10 to −14 W m^{-2} range for hemispheric/seasonal and also for global/annual averages. Values in Table 2 also show that overestimation in net SW combined with underestimation in net LW leads to a good agreement in the values of net total flux. Interestingly, similar compensation between net SW and net LW fluxes was also found in the simulations with the GCM of the Max Planck Institute for Meteorology (ECHAM3) when compared with surface measured fluxes from GEBA (Wild et al. 1995).

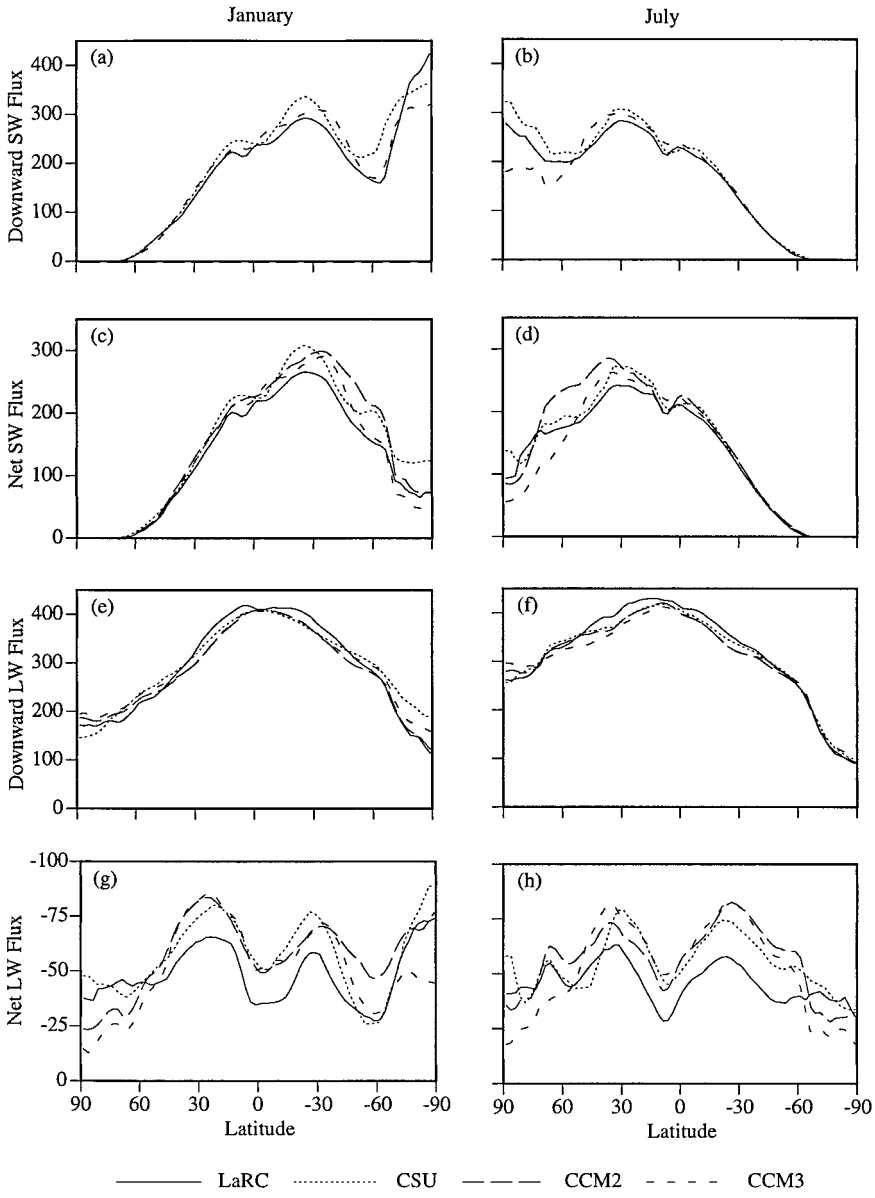

FIG. 14. Comparisons of the climatological means of zonally averaged surface radiative fluxes from the GCMs with those from the LaRC dataset for Jan and Jul.

b. CCM2

The CCM2 results compared here also came from the 10-yr simulations produced for the AMIP using the model described by Hack et al. (1993). The CCM2 dataset was acquired from the Program for Climate Model Diagnosis and Intercomparison at the Lawrence Livermore National Laboratory, where it was produced and is archived (P. Gleckler 1997, personal communication). Downward SW and LW fluxes were not archived in these simulations. Downward LW fluxes were recreated in the present work using surface temperature and net LW flux fields, assuming surface emissivity to be unity. Downward SW flux fields were not recreated because surface albedo fields were not available. Differences for all available SRB parameters from CCM2 are presented in the middle three columns of Table 2.

Global-annual average net SW flux in CCM2 exceeds the LaRC value by about 19 W m^{-2}, while hemispheric/seasonal differences range from 7 to 34 W m^{-2}. Differences for DLF and NLF range from -11 to -18 W m^{-2} for all averages. As for many other GCMs, overestimation in net SW compensates for underestimation in net LW to yield a good agreement for net total flux. Ward (1995) conducted detailed comparisons of surface SW fluxes from CCM2 with satellite-derived fluxes from the WCRP/SRB version 1.1 dataset (Whitlock et

TABLE 2. Differences between hemispheric and global climatological average surface radiative fluxes from each of the GCMs with those from the LaRC dataset (W m^{-2}) for Jan, Jul, and whole year.

	CSU − LaRC			CCM2 − LaRC			CCM3 − LaRC		
	NH	SH	Global	NH	SH	Global	NH	SH	Global
				Downward shortwave flux					
Jan	11.0	29.4	20.2	—	—	—	6.0	16.6	11.3
Jul	15.3	3.9	9.6	—	—	—	7.1	2.7	4.8
Annual	15.6	17.9	16.7	—	—	—	7.7	11.8	9.7
				Net shortwave flux					
Jan	12.9	28.8	20.8	10.6	34.0	22.3	6.8	17.1	11.9
Jul	15.4	4.6	10.1	29.0	7.0	18.1	7.1	3.8	5.5
Annual	17.2	17.4	17.3	18.9	20.0	19.4	8.8	11.9	10.3
				Downward longwave flux					
Jan	−2.7	−4.3	−3.5	−12.9	−12.5	−12.7	−9.0	−8.0	−8.5
Jul	−10.9	−6.5	−8.7	−13.1	−15.1	−14.1	−22.9	−12.0	−17.3
Annual	−7.3	−7.4	−7.4	−15.8	−15.4	−15.6	−15.9	−11.9	−13.9
				Net longwave flux					
Jan	−10.2	−12.8	−11.5	−10.5	−16.1	−13.3	−9.3	−11.2	−10.2
Jul	−10.1	−13.7	−11.8	−10.8	−18.4	−14.6	−12.0	−16.5	−14.2
Annual	−10.8	−14.3	−12.5	−11.6	−17.8	−14.7	−10.9	−15.0	−12.9
				Net total (SW + LW) flux					
Jan	2.7	16.0	9.3	0.1	17.9	9.0	−2.5	5.9	1.7
Jul	5.3	−9.1	−1.7	18.2	−11.4	3.5	−4.9	−12.7	−8.7
Annual	6.4	3.1	4.8	7.3	2.2	4.7	−2.1	−3.1	−2.6

al. 1995) produced with the Pinker algorithm (Pinker and Laszlo 1992). Regional comparisons by Ward (1995) showed overestimation in CCM2 by as much as 100 W m^{-2} in some regions. These differences were attributed primarily to deficiencies in cloud amounts and cloud optical depths in CCM2 and also to the omission of aerosol effects to a smaller extent. The same factors may also account for the underestimation of DLF and NLF in CCM2, even though definite conclusions cannot be drawn at this time from the limited LW comparisons presented here.

c. CCM3

The CCM3 results compared here were produced in a 5-yr simulation (January 1985–December 1989) carried out at the State University of New York (SUNY) at Stony Brook and were acquired from SUNY (M. Zhang 1997, personal communication). The CCM3 is the newest version of the NCAR/CCM and is described by Kiehl et al. (1996). Improvements made to the CCM3 are in the inclusion of background aerosols and in the diagnosis of cloud particle size and liquid water path, among other things. The differences for climatological average SRB parameters from CCM3 based on the 5-yr dataset are presented in the last three columns of Table 2. These numbers show that downward and net SW fluxes in CCM3 still have positive biases, but the magnitudes of these biases are about half those found for CCM2. Global annual bias for both downward and net SW fluxes is about 10 W m^{-2}, and the hemispheric-seasonal biases range from 3 to 17 W m^{-2}. For CCM3 simulations also, DLF values were not archived and were recreated using the same procedure as for CCM2. Comparisons for DLF and NLF show that the improvements for these fluxes relative to CCM2 are quite small. Biases in DLF and NLF are −14 and −13 W m^{-2}, respectively, for global anual averages and range from −8 to −23 W m^{-2} for hemispheric/seasonal averages. Net total fluxes for CCM3 show small negative biases as the magnitudes of biases in the LW fluxes now exceed those in the SW fluxes. The improvements in the values of fluxes (and biases) for CCM3 are consistent with the improvements in cloud amounts diagnosed in CCM3 (not shown here), which are now closer to the ISCCP values.

d. Atmospheric SW absorption

Absorption of SW radiation in the atmospheric column is directly related to the diabatic heating and general circulation of the atmosphere (Kiehl et al. 1995) and is an important parameter diagnosed in the GCMs. Comparisons presented earlier in this paper did not cover this parameter because it is not a part of the SRB. The SW SRB parameters of the LaRC dataset, in conjunction with TOA SW parameters from ERBE, are used to estimate this parameter, which is then used for comparisons of the corresponding values diagnosed in the GCMs. Global annual average value of atmospheric SW absorption derived using the surface net SW flux from Table 1 (160.9 W m^{-2}), a solar constant of 1365 W m^{-2} (used in the present work and also for ERBE), and the TOA-reflected SW flux from ERBE (102.2 W m^{-2}) are presented in Table 3. Corresponding values obtained from the three GCMs along with values of surface SW absorption from all sources are also shown. Values in Table 3 show that all GCMs underestimate atmospheric

TABLE 3. Comparison of the absorption of solar radiation at the surface and in the atmosphere. Fluxes are in W m^{-2}. Numbers in parentheses are percentages of TOA insolation.

Model	Solar constant	Absorbed at the surface	Absorbed in the atmosphere
LaRC	1365	160.9 (47.2)	78.2 (22.9)
CSU	1365	178.2 (52.2)	60.5 (17.7)
CCM2	1370	180.3 (52.6)	67.6 (19.7)
CCM3	1367	171.2 (50.1)	65.8 (19.3)

SW absorption significantly, while they overestimate surface SW absorption. Li et al. (1997) performed a similar comparison among four observational (and quasi-observational) datasets and four GCMs (including CSU/GCM and CCM2) in the context of solar energy disposition in the surface–atmosphere system. Li et al. concluded that, compared to the observations, GCMs significantly underestimated atmospheric absorption and overestimated surface absorption by about the same amount, as most GCMs match the observations quite well at the TOA. Values derived from the LaRC dataset show good agreement with those derived from observational data and thus support the conclusions drawn by Li et al. (1997).

7. Discussion of errors

Errors in the satellite fluxes presented here, which are derived using radiation models with satellite meteorological data, arise from both the models and the satellite data. The radiation models contribute primarily to the biases (systematic errors) because of the processes not included in the models, errors in the radiative parameters (e.g., absorption coefficients), and other assumptions and approximations made in the implementation of the models. Errors in the input data propagate to the computed fluxes and contribute to both systematic and random errors. All errors in satellite fluxes are highly variable spatially and temporally and are different for SW and LW fluxes. When these fluxes are compared with site measurements, it is convenient to attribute all differences to errors in the satellite results. That is not the case, however, because site measurements are subject to biases and random errors of their own. All of these sources of error are discussed below for both SW and LW fluxes.

A major source of error for the satellite SW fluxes is in the computation of cloud transmittances from scaled visible radiances of the C1 data (Darnell et al. 1992). Two factors contribute to the errors in cloud transmittances. First, the C1 visible radiances are subject to a 7%–10% uncertainty from the calibration of visible channels on the NOAA polar orbiters and the geostationary satellites (Whitlock et al. 1995). Second, the use of narrowband radiances to infer broadband cloud transmittances introduces additional errors in all computations for cloudy conditions. Some of the differences between satellite and site fluxes seen at the Payerne site may be due to this deficiency in the SW model. Another source of error in the SW fluxes is in the accounting for aerosol extinction. Average values of aerosol radiative properties for a few common aerosol types (see appendix) are used in the model. The lack of consideration of local aerosol characteristics may contribute to significant errors over dusty and/or polluted areas. The differences between satellite and site insolation values for the August–December period at the Manaus site shown in Fig. 11b may be occurring because of absorbing aerosols from biomass burning in the region that are not accounted for in the model. Net SW fluxes are affected further by the uncertainties in the surface albedos used in the model, which may be especially large over snow/ice-covered regions. Errors are also contributed to the SW fluxes by uncertainties in column water vapor and ozone burdens. Comparisons between site and satellite fluxes are also affected by errors in the site fluxes. Using sources from the literature, Garratt (1994) estimated random error for monthly average site fluxes to be about 5 W m^{-2} for those sites where the pyranometers were well maintained and clean. For a larger, more representative set of sites, Garratt (1994) analyzed the differences between neighboring sites and estimated the uncertainty to be about 11 W m^{-2} for monthly averages. Interestingly, this value is very close to the rms difference between satellite and site fluxes for the three multisite boxes over Germany as shown in Fig. 13b. Based on the comparisons presented in section 5, uncertainties in the present SW fluxes are estimated to be about 15 W m^{-2} in the monthly average, but they are highly variable geographically.

Many assumptions made in the LW model used in the present work contribute to the errors in satellite LW fluxes. Treatment of clouds as plane-parallel single-layer blackbodies is a major source of errors for satellite DLF. Specifically, the deficiencies in satellite-derived cloud properties contribute significantly to these errors. These deficiencies include the underestimation of low clouds in the presence of high clouds and the inability to detect fog. Also, cloud-base heights are estimated from cloud-top heights and climatological values of cloud thickness. One or more of these deficiencies may be contributing to the large underestimation of satellite DLF at the Hamburg site seen in Fig. 12c. The effects of cloud emissivity errors (the assumption of black clouds) should be small because low and middle clouds are nearly black and high clouds have little effect on DLF. The effect of surface emissivity deviation from unity, however, contributes significant biases to net LW flux, particularly over desert regions where surface emissivity is substantially less than unity. For a complete analysis of errors in the surface LW fluxes derived from satellite data, the reader is referred to Gupta et al. (1993b). For

regions where meteorological inputs are well defined, the errors in satellite DLF were estimated to be 5–15 W m^{-2}. For regions with larger uncertainties in meteorological inputs, the errors in fluxes would be correspondingly higher. Also, the comparisons between site and satellite fluxes presented in section 5 are subject to measurement errors in the site fluxes. Garratt and Prata (1996) analyzed the uncertainties in site-measured DLF and estimated that monthly averages should be reliable within about 5 W m^{-2} for sites where pyrgeometers are well maintained and the dome heating correction was properly applied. Based on the comparisons of LW fluxes presented in section 5, estimated uncertainty in the present LW fluxes is again about 15 W m^{-2} for the monthly average, and they are highly variable geographically.

8. Concluding remarks

Climatologies of SRB parameters on a global scale are highly desirable for studies of climate processes, and for initialization and validation of GCMs (Suttles and Ohring 1986). This paper presents climatologies of downward and net SW and LW fluxes at the surface on a global scale for each month of the year. These climatologies are based on a time series of monthly average fluxes for a period of 96 months (8 yr) derived from validated radiative transfer parameterizations (Darnell et al. 1992; Gupta et al. 1992) and satellite meteorological inputs obtained primarily from the ISCCP (Rossow and Schiffer 1991). SRB parameters derived indirectly from satellite data (as in the present work) may be the only method for deriving them on a global scale, because (i) surface fluxes do not lend themselves to direct measurement by satellites, and (ii) uniform global coverage can only be achieved with satellite observations. By comparison, datasets based on surface observations are greatly limited in spatial coverage (mostly to NH land areas) and do not provide all parameters. Also, measurements made at different places may have significant biases because of the differences between instruments and because of operation and calibration procedures.

Examination of the results presented in section 4 shows that the time series and the geographical and zonally averaged distributions are consistent with the underlying meteorological inputs and with our best understanding of the physical processes occurring in the system. The strong correspondence between surface and TOA anomalies for both SW and LW fluxes during the 1986/87 ENSO episode greatly enhances confidence in the present results. Recall that the TOA anomalies were derived from ERBE observations (Harrison et al. 1994), which are completely independent of the present work. Comparisons presented in section 5 show that the present results agree well with site measurements at most places most of the time. In many cases, where significant differences occur, the differences can be associated with known deficiencies in the surface measurements and/or the satellite-derived inputs. There were cases, however, where the differences could not be explained in terms of identifiable causes. The scatterplot in Fig. 13b, of the comparison for three grid boxes over Germany gives a good indication of the quality of the LaRC results under optimum conditions. The surface measurements used in this case are regarded as high quality, and the averaging of several sites in each grid box alleviates the effects of the spatial mismatch between grid box and site data. Under such conditions, the LaRC results come close to meeting the accuracy requirement for climate research, which is about 10 W m^{-2} for regional monthly averages (Suttles and Ohring 1986).

Comparisons of downward and net SW fluxes with results of three GCMs show that the LaRC estimates are consistently lower than the GCM values by 10–20 W m^{-2} but in better agreement with those derived from other satellite algorithms (Li et al. 1997) and with surface measurements (Wild et al. 1995). Comparisons of DLF show that the LaRC values are 10–15 W m^{-2} higher than the GCM values. These differences are similar to those found by Wild et al. (1995) between results of ECHAM3 and surface measurements.

Recognizing the importance of this dataset for climate research, and to encourage its use and scrutiny by the science community, it has been made available to the community in several ways. It can be accessed on the World Wide Web at http://srb-swlw.larc.nasa.gov/. It can also be obrained on a CD-ROM by sending requests to Dr. Paul W. Stackhouse Jr., Mail Stop 420, NASA/Langley Research Center, Hampton, VA 23681-2199.

Acknowledgments. The authors are grateful to E. Dutton, J. Garratt, M. Wild, and T. Konzelmann for providing several datasets of surface measurements and to D. Randall, P. Gleckler, and M. Zhang for the GCM datasets. The authors are also grateful to D. Kratz and two anonymous reviewers for many valuable comments and suggestions, all of which have resulted in improvement of the paper.

APPENDIX

Augmentation of the SW Model

The SW model used in the present work has been augmented in two significant ways from that described in Darnell et al. (1992). The aerosol attenuation factor in Darnell et al. (1992) was evaluated as a residual and was dependent on the water vapor burden of the atmosphere. In the present model, the attenuation factor is computed using radiative parameters from climatological data available for standard types of aerosols (Deepak and Gerber 1983), with minor adjustments over some areas based on data from local measurements. Also, the computation of land surface albedo has been modified to take advantage of the long-term ERBE TOA

TABLE A1. Aerosol radiative parameters τ, g, and ω for the five scene types.

Scene type	Aerosol type	τ	g	ω
Ocean	Maritime	$0.15U_e$	0.60	0.95
Land	Continental	$0.35U_e$	0.66	0.90
Desert	Desert	$(0.3 + 0.5A_t)U_e$	0.60	0.92
Coast	50/50 Maritime and Continental	$0.25U_e$	0.64	0.92
Snow/ice	Snow/ice	0.03	0.67	0.97

broadband measurements. Both enhancements are briefly described below.

a. Aerosol attenuation

The aerosol attenuation factor in the present model is computed as

$$\alpha_{\text{Aerosol}} = \tau(1 - \omega) + \tau(1 - g)/2, \qquad (1)$$

where τ is the ''effective broadband'' aerosol optical depth, ω is the single scattering albedo, and g is the asymmetry factor. The first term on the right accounts for the absorption of downward SW radiation, and the second term accounts for upward reflection or the backscattered radiation. Forward scattering of the downward radiation by aerosols is not considered. A standard aerosol type (or a combination) was associated with each of the five scene types used in this work. These associations and average values of the radiative parameters τ, g, and ω for each scene type are presented in Table A1. Here, A_t (in Table A1) represents the monthly average ERBE TOA clear-sky albedo for the grid box. The value U_e (also in Table A1) is the effective daily value of the cosine of solar zenith angle for the grid box, averaged from sunrise to sunset; U_e is defined in accordance with the value of the ratio F/G as follows:

$$U_e = F + G[(G - F)/2G]^{0.5}$$

for $-1 < F/G < 1$, which applies over most of the globe, $U_e = F$ for $F/G > 1$ (polar day areas), and U_e is undefined for $F/G < -1$ (polar night areas). In the definitions above, $F = \sin(\text{elat}) \times \sin(\text{sdec})$ and $G = \cos(\text{elat}) \times \cos(\text{sdec})$, where elat is the latitude of the areal center and sdec is the daily averaged solar declination for the grid box.

b. Clear-sky land surface albedos

Clear-sky surface albedos over land areas were derived from corresponding TOA albedos with the Staylor and Wilber (1990) approach. This approach modified the Koepke and Kriebel (1987) linear relationship between surface and TOA albedos to compute daily averages instead of instantaneous values. The source of TOA albedos changed depending on the snow/ice condition at the surface. For land areas that are snow/ice free throughout a month, monthly average clear-sky broadband TOA albedos from ERBE measurements were used for every day of the month. For land areas that are snow/ice covered during all or part of a month, the ERBE monthly average value was used for snow/ice-free days of the month. For snow/ice-covered days of that month, clear-sky TOA albedos were constituted from the lowest daily TOA reflectances available from C1 data, a method that was also used over ice-covered ocean areas. The ERBE data cover the period March 1985–December 1988 and were used as such for those 46 months. The ERBE monthly average TOA albedos over this period show less than 1% interannual variability on a month-by-month basis. Therefore, multiyear monthly averages of these albedos from the ERBE period were also used for the corresponding months outside the ERBE period. Other parts of the albedo algorithm remain consistent with Darnell et al. (1992).

REFERENCES

Arking, A., M.-D. Chou, and W. L. Ridgway, 1996: On estimating the effect of clouds on atmospheric absorption based on flux observations above and below cloud level. *Geophys. Res. Lett.,* **23,** 829–832.

Barkstrom, B., E. Harrison, G. Smith, R. Green, J. Kibler, R. Cess, and the ERBE Science Team, 1989: Earth Radiation Budget Experiment (ERBE) archival and April 1985 results. *Bull. Amer. Meteor. Soc.,* **70,** 1254–1262.

Cahoon, D. R., B. J. Stocks, J. S. Levine, W. R. Cofer III, and K. P. O'Neill, 1992: Seasonal distribution of African savanna fires. *Nature,* **359,** 812–815.

Cess, R. D., E. G. Dutton, J. J. DeLuisi, and F. Jiang, 1991: Determining surface solar absorption from broadband satellite measurements for clear skies: Comparison with surface measurements. *J. Climate,* **4,** 236–247.

——, and Coauthors, 1995: Absorption of solar radiaton by clouds: Observations versus models. *Science,* **267,** 496–499.

Chou, M.-D., A. Arking, J. Otterman, and W. L. Ridgway, 1995: The effect of clouds on atmospheric absorption of solar radiation. *Geophys. Res. Lett.,* **22,** 1885–1888.

Darnell, W. L., S. K. Gupta, and W. F. Staylor, 1983: Downward longwave radiation at the surface from satellite measurements. *J. Climate Appl. Meteor.,* **22,** 1956–1960.

——, ——, and ——, 1986: Downward longwave surface radiation from sun-synchronous satellite data: Validation of methodology. *J. Climate Appl. Meteor.,* **25,** 1012–1021.

——, W. F. Staylor, S. K. Gupta, and F. M. Denn, 1988: Estimation of surface insolation using sun-synchronous satellite data. *J. Climate,* **1,** 820–835.

——, ——, ——, N. A. Ritchey, and A. C. Wilber, 1992: Seasonal variation of surface radiation budget derived from ISCCP-C1 data. *J. Geophys. Res.,* **97,** 15 741–15 760.

Deepak, A., and H. E. Gerber, Eds., 1983: Report of the experts meeting on aerosols and their climatic effects. WCP-55, 107 pp.

Fowler, L. D., and D. A. Randall, 1996: Liquid and ice cloud microphysics in the CSU general circulation model. Part II: Impact on cloudiness, the earth's radiation budget, and the general circulation of the atmosphere. *J. Climate,* **9,** 530–560.

——, ——, and S. A. Rutledge, 1996: Liquid and ice cloud microphysics in the CSU general circulation model. Part I: Model description and simulated microphysical processes. *J. Climate,* **9,** 489–529.

Garratt, J. R., 1994: Incoming shortwave fluxes at the surface—A comparison of GCM results with observations. *J. Climate,* **7,** 72–80.

——, and A. J. Prata, 1996: Downwelling longwave fluxes at con-

tinental surfaces—A comparison of observations with GCM simulations and implications for the global land-surface radiation budget. *J. Climate,* **9,** 646–655.
Gates, W. L., 1992: AMIP: The atmospheric model intercomparison project. *Bull. Amer. Meteor. Soc.,* **73,** 1962–1970.
Gautier, C., G. Diak, and S. Masse, 1980: A simple physical model to estimate incident solar radiation at the surface from GOES satellite data. *J. Appl. Meteor.,* **19,** 1005–1012.
Gupta, S. K., 1983: A radiative transfer model for surface radiation budget studies. *J. Quant. Spectrosc. Radiat. Transfer,* **29,** 419–427.
——, 1989: A parameterization for longwave surface radiation from sun-synchronous satellite data. *J. Climate,* **2,** 305–320.
——, W. L. Darnell, and A. C. Wilber, 1992: A parameterization for longwave surface radiation from satellite data: Recent improvements. *J. Appl. Meteor.,* **31,** 1361–1367.
——, W. F. Staylor, W. L. Darnell, A. C. Wilber, and N. A. Ritchey, 1993a: Seasonal variation of surface and atmospheric cloud radiative forcing over the globe derived from satellite data. *J. Geophys. Res.,* **98,** 20 761–20 778.
——, A. C. Wilber, W. L. Darnell, and J. T. Suttles, 1993b: Longwave surface radiation over the globe from satellite data: An error analysis. *Int. J. Remote Sens.,* **14,** 95–114.
Hack, J. J., B. A. Boville, B. P. Briegleb, J. T. Kiehl, P. J. Rasch, and D. L. Williamson, 1993: Description of the NCAR Community Climate Model (CCM2). NCAR Tech. Note NCAR/TN-382+STR, 108 pp.
Harrison, E. F., P. Minnis, G. G. Gibson, F. M. Denn, and D. R. Doelling, 1994: Earth Radiation Budget Experiment observations of the 1987 and 1992 ENSO events. Preprints, *Sixth Conf. on Climate Variations,* Nashville, TN, Amer. Meteor. Soc., 336–340.
Kiehl, J. T., J. J. Hack, M. H. Zhang, and R. D. Cess, 1995: Sensitivity of a GCM climate to enhanced shortwave cloud absorption. *J. Climate,* **8,** 2200–2212.
——, ——, G. B. Bonan, B. A. Boville, B. P. Briegleb, D. L. Williamson, and P. J. Rasch, 1996: Description of the NCAR Community Climate Model (CCM3). NCAR Tech. Note NCAR/TN-420+STR, 152 pp.
Koepke, P., and K. T. Kriebel, 1987: Improvements in the shortwave cloud-free radiation budget accuracy. Part I: Numerical study including surface anisotropy. *J. Climate Appl. Meteor.,* **26,** 374–395.
Konzelmann, T., D. R. Cahoon, and C. H. Whitlock, 1996: Impact of biomass burning in equatorial Africa on the downward surface shortwave irradiance: Observations versus calculations. *J. Geophys. Res.,* **101,** 22 833–22 844.
Kousky, V. E., and A. Leetmaa, 1989: The 1986–87 Pacific warm episode: Evolution of oceanic and atmospheric anomaly fields. *J. Climate,* **2,** 254–267.
Li, Z., H. G. Leighton, and R. D. Cess, 1993: Surface net solar radiation estimated from satellite measurements: Comparisons with tower observations. *J. Climate,* **6,** 1764–1772.
——, H. W. Barker, and L. Moreau, 1995: The variable effect of clouds on atmospheric absorption of solar radiation. *Nature,* **376,** 486–490.
——, L. Moreau, and A. Arking, 1997: On solar energy disposition: A perspective from observation and modeling. *Bull. Amer. Meteor. Soc.,* **78,** 53–70.
Ohmura, A., and H. Gilgen, 1991: Global Energy Balance Archive (GEBA), World Climate Program–Water Project A7, Rep. 2: The GEBA data base, interactive applications, retrieving data. *Zuercher Geographische Schriften, 44,* 66 pp.
——, and ——, 1993: Re-evaluation of the global energy balance. Interactions between global climate subsystems: The legacy of Hann. *Geophys. Monogr.,* No. 75, International Union of Geodesy and Geophysics, 93–110.
Payne, R. E., 1972: Albedo of the sea surface. *J. Atmos. Sci.,* **29,** 959–970.
Philander, S. G., 1990: *El Nino, La Nina, and the Southern Oscillation.* Academic Press, 289 pp.
Pilewskie, P., and F. P. J. Valero, 1995: Direct observations of excess solar absorption by clouds. *Science,* **267,** 1626–1629.
Pinker, R. T., and J. A. Ewing, 1985: Modeling surface solar radiation: Model formulation and validation. *J. Climate Appl. Meteor.,* **24,** 389–401.
——, and I. Laszlo, 1992: Modeling surface solar irradiance for satellite applications on a global scale. *J. Appl. Meteor.,* **31,** 194–211.
Ramanathan, V., 1986: Scientific use of surface radiation budget for climate studies. Surface Radiation Budget for Climate Applications. NASA RP-1169, 58–86.
——, B. Subasilar, G. J. Zhang, W. Conant, R. D. Cess, J. T. Kiehl, H. Grassl, and L. Shi, 1995: Warm pool heat budget and shortwave cloud forcing: A missing physics. *Science,* **267,** 499–503.
Rossow, W. B., and R. A. Schiffer, 1991: ISCCP cloud data products. *Bull. Amer. Meteor. Soc.,* **72,** 2–20.
——, L. C. Garder, P. J. Lu, and A. Walker, 1988: International Satellite Cloud Climatology Project (ISCCP): Documentation of cloud data. WMO/TD 266, World Climate Research Programme, Geneva, Switzerland, 75 pp.
Schmetz, J., 1989: Towards a surface radiation climatology: Retrieval of downward irradiance from satellites. *Atmos. Res.,* **23,** 287–321.
Schmetz, P., J. Schmetz, and E. Raschke, 1986: Estimation of daytime longwave radiation at the surface from satellite and grid point data. *Theor. Appl. Climatol.,* **37,** 136–149.
Staylor, W. F., and A. C. Wilber, 1990: Global surface albedos estimated from ERBE data. Preprints, *Seventh Conf. on Atmospheric Radiation,* San Francisco, CA, Amer. Meteor. Soc., 231–236.
Stephens, G. L., and P. J. Webster, 1984: Cloud decoupling of the surface and planetary radiative budgets. *J. Atmos. Sci.,* **41,** 681–686.
——, A. Slingo, M. J. Webb, P. J. Minnett, P. H. Daum. L. Kleinman, I. Wittmeyer, and D. A. Randall, 1994: Observations of the Earth's radiation budget in relation to atmospheric hydrology. 4. Atmospheric column radiative cooling over the world's oceans. *J. Geophys. Res.,* **99,** 18 585–18 604.
Suttles, J. T., and G. Ohring, 1986: Surface radiation budget for climate applications. NASA Reference Publication 1169, NASA, Washington, DC, 132 pp.
Tarpley, J. D., 1979: Estimating incident solar radiation at the surface from geostationary satellite data. *J. Appl. Meteor.,* **18,** 1172–1181.
Telegadas, K., and J. London, 1954: A physical model of the Northern Hemisphere troposphere for winter and summer. Scientific Rep. 1, Dept. of Meteorology and Oceanography, New York University, 55 pp.
Trenberth, K. E., 1997: The definition of El Niño. *Bull. Amer. Meteor. Soc.,* **78,** 2771–2777.
Ward, D. M., 1995: Comparison of the surface solar radiation budget derived from satellite data with that simulated by the NCAR CCM2. *J. Climate,* **8,** 2824–2842.
Warren, S. G., C. J. Hahn, J. London, R. M. Chervin, and R. L. Jenne, 1986: Global distribution of total cloud cover and cloud type amounts over land. NCAR Tech. Note NCAR/TN-273+STR, 29 pp.
Whitlock, C. H., T. P. Charlock, W. F. Staylor, R. T. Pinker, I. Laszlo, R. C. DiPasquale, and N. A. Ritchey, 1993: WCRP surface radiation budget shortwave data product description-Version 1.1. NASA Tech. Memo. 107747, 28 pp.
——, and Coathors, 1995: First global WCRP shortwave surface radiation budget dataset. *Bull. Amer. Meteor. Soc.,* **76,** 905–922.
Wild, M., A. Ohmura, H. Gilgen, and E. Roeckner, 1995: Validation of general circulation model radiative fluxes using surface observations. *J. Climate,* **8,** 1309–1324.
Wittmeyer, I. L., and T. H. Vonder Haar, 1994: Analysis of the global ISCCP TOVS water vapor climatology. *J. Climate,* **7,** 325–333.
WCRP-69, 1992: Radiation and climate: Report of the fourth session of the WCRP working group on radiative fluxes. WMO/TD-No. 471.